RSC Advances

PAPER

View Article Online
View Journal | View Issue

Cite this: *RSC Adv.*, 2024, **14**, 15722

Enhancing the electrochemical properties of $TiNb_2O_7$ anodes with SP-CNT binary conductive agents for both liquid and solid state lithium ion batteries†

Li-Qian Cheng, [a] Xinyuan Xie,[a] Kai Chen, *[b] Yijuan He,[a] Hu Xu,[a] Ruiping Liu [a] and Ming Feng *[c]

A high performance oxide composite electrode is obtained with a two-step solid state calcined titanium niobium oxide $TiNb_2O_7$ (TNO) anode and super P-carbon nanotube (SP-CNT) binary conductive agents. The solid state synthesized TNO-0.2C (the proportion of CNTs in the binary conductive agent is 20% wt) anode exhibits a high reversible discharge capacity of 278.6 mA h g^{-1} at 0.5C, a competitive rate capability with reported works that employed wet chemical methods at moderate rates (178.1 mA h g^{-1} at 10C), and an excellent capacity retention of 92.2% after 200 cycles at 1.5C/1.5C. The enhancement in electrochemical properties of the TNO-0.2C anode is mainly attributed to the combination of the short range and long range conductive agents in the SP-CNT binary conductive system, which guarantees an efficient electronic conductive network. The $Li|Li_{1.3}Al_{0.3}Ti_{1.7}(PO_4)_3$ composite polymer electrolyte ($LATP_{CPEs}$)|TNO-0.2C solid state batteries are also assembled, which deliver a high initial reversible discharge capacity of 241.3 mA h g^{-1} at 1C and a good capacity retention rate of 93% after 50 cycles. This work provides an efficient way to improve the electrochemical properties of TNO anodes in lithium ion batteries, especially for solid state batteries.

Received 23rd March 2024
Accepted 6th May 2024

DOI: 10.1039/d4ra02216e

rsc.li/rsc-advances

Introduction

Lithium ion batteries (LIBs) are regarded as the most promising energy storage technology due to their long cycle life and high energy density. LIBs are widely used in portable electronic devices, such as laptops, mobile phones, and digital cameras.[1,2] Moreover, attributed to the inevitable environmental pollution caused by motor vehicles, the research and development of pure electric vehicles (EVs) and hybrid electric vehicles (HEVs) have been strongly encouraged.[3,4] LIBs are considered to be electrochemical energy storage systems that can provide energy for EVs and HEVs.[5] However, they put forward higher requirements for battery durability, charging rate, service life, and safety.[6] Commercial LIBs usually use graphite as the anode material. However, due to its low lithium intercalation potential (~0.1 V *vs.* Li/Li^+), the solid-electrolyte interphase (SEI) layer and lithium dendrites will inevitably be generated during the charge/discharge process, resulting in lower coulomb efficiency and increased safety risks.[7,8] For comparison, an alternative anode material such as lithium titanate (LTO) has attracted the attention of researchers, which features a "zero-strain" structure with a high intercalation potential (~1.57 V *vs.* Li/Li^+).[9] High potential can effectively avoid the formation of SEI and harmful lithium dendrites; the "zero-strain" characteristic makes LTO achieve good cyclic stability. However, the low theoretical capacity (175 mA h g^{-1}) of the LTO anode limits its application potential in high-power applications.[10]

Titanium niobium oxides such as $TiNb_2O_7$ and $Ti_2Nb_{10}O_{29}$ recently emerge as new promising active materials for replacing LTO in LIBs,[11] TNO has three redox couples including Ti^{4+}/Ti^{3+}, Nb^{5+}/Nb^{4+}, and Nb^{4+}/Nb^{3+}, and possesses a high theoretical capacity of 387.6 mA h g^{-1}.[12] In addition, the lithium intercalation potential of TNO is about 1.6 V, matching the lowest unoccupied molecular orbital (LUMO) of the organic liquid-carbonate electrolyte, leading to high coulomb efficiency and safety. What's more, a majority of solid electrolyte with high ionic conductivity for solid state batteries, such as sulfide electrolyte,[13,14] halide electrolyte,[15,16] and oxide electrolyte with titanium element,[17,18] are not stable at low potential. Thus, TNO is also a promising high performance anode material for solid state batteries. Unfortunately, TNO has the defects of poor

[a]*Department of Materials Science and Engineering, China University of Mining & Technology, Beijing, 100083, China*

[b]*QingTao (Kunshan) Energy Development Co., Ltd, Suzhou, 215334, China. E-mail: chenkai_qingtao@163.com*

[c]*Key Laboratory of Functional Materials Physics and Chemistry of the Ministry of Education, Jilin Normal University, Changchun, 130103, China. E-mail: mingfeng@jlnu.edu.cn*

† Electronic supplementary information (ESI) available. See DOI: https://doi.org/10.1039/d4ra02216e

intrinsic electronic conductivity and ionic conductivity.[19] Moreover, its lithium ion diffusion coefficient is not very satisfactory.[20] The main goal is to improve the reaction kinetics of TNO. At present, researchers have done a lot to solve this problem. Common approaches include reducing particle size,[21–24] doping heteroatoms[25–27] to change crystal structure and forming composites with conductive phases.[20,28–30] These reports have significantly improved the electrochemical performance of TNO. However, they all focus on the modification of active materials, which still have a series of problems such as complex operation and high cost.

The electrode of LIBs is usually prepared by casting a slurry of the active materials, conductive agents, and binder onto a metallic current collector.[31,32] The role of the conductive agent in the electrode is to provide a channel for electron transmission, improves the electron transmission coefficient in the LIBs and reduce the charge transfer resistance of the electrode.[32–35] Appropriate amounts, types, and proportion of conductive agents can achieve higher discharge capacity and better cycle performance. The traditional conductive agents for LIBs are mainly carbon materials such as Super P (SP) and acetylene black (AB). Compared to single conductive agents, binary conductive agents can build a more efficient conductive network and improve the electron transmission coefficient. Wang *et al.*[36] combined SACNT with SP to build binary conductive agents, which considered the advantages of SACNT long range conductive path and SP short range conductive path. The binary conductive agents can enhance the mechanical strength of the electrode and significantly improve electrochemical performance. Zhang *et al.*[37] taken a pairwise coupling of SP, CNTs, and GNs into binary carbon-based conductive. The results showed that the binary conductive agents can provide a more efficient conductive network and a faster lithium ion transmission cathode system compared with traditional conductive agents. Cheon *et al.*[38] used SP and Lonza-KS6 as the binary conductive agents, the results showed that the batteries containing binary conductive agents have better cycle life than those using single conductive agents. Cao *et al.*[39] employed SP-CNT binary conductive agent and effectively improved the electrochemical performance of NCM cathode. The SP-CNT binary conductive agent exhibited a larger specific surface area and build an efficient composite conductive network, which is an effective way to prepare high-performance electrodes. Thus, introducing binary conductive agents will be a promising method to enhance the electrochemical properties of TNO anodes.

Herein, the two-step solid state calcined TNO is chosen as the active material, which possesses excellent cycling performance as reported in our previous work.[40] And the SP-CNT binary conductive agents are introduced to enhance the electrochemical properties of the TNO composite anode. The combination of the short range and long range conductive agents guarantee an efficient electronic conductive network and bring great electrochemical performances. The solid state synthesized TNO-C anode exhibits high reversible discharge capacity, competitive rate capabilities with those reported works employed wet chemical methods at moderate rates, and excellent cycling stability. The Li|$LATP_{CPEs}$|TNO-0.2C solid state batteries are also assembled, which delivers high reversible discharge capacities, excellent rate capabilities and good cycling performances. Therefore, the addition of the SP-CNT binary conductive agents is a high efficient way to improve the electrochemical properties of high-performance oxide composite electrode, especially for solid state batteries.

Experimental

Preparation of materials

Preparation of TNO powders. $TiNb_2O_7$ material was prepared by a facile two-step solid state method as reported in our previous work.[40] TiO_2 (≥99%) and $Nb(OH)_5$ (99.95%) were used as starting materials with a molar ratio of 1 : 2. The raw materials were mixed in ethanol with ball milling for 12 h. Then the dried mixture was calcined in a muffle furnace at 1100 °C for 8 h, and ball milled again. After that, the dried powder was calcined again in a muffle furnace at 1000 °C for 8 h and crushed by ball milling.

Preparation of TNO composite electrodes. The TNO composite electrodes were prepared by mixing the active material, binder (polyvinylidene fluoride, PVDF), and SP-CNT binary conductive agents in a weight ratio of 8 : 1 : 1 in *N*-methyl-2-pyrrolidinone (NMP). The slurry was then coated on Al foil and dried in an oven at 80 °C for 12 h. The SP-CNT binary conductive agents consist of CNTs and SP with weight ratios of 0.05 : 0.95, 0.1 : 0.9, 0.15 : 0.85, 0.2 : 0.8 and 0.5 : 0.5, which are marked as TNO-0.05C, TNO-0.1C, TNO-0.15C, TNO-0.2C and TNO-0.5C, respectively.

Preparation of LATP/PVDF/g-C_3N_4 CPEs. The LATP-based composite polymer electrolytes ($LATP_{CPEs}$) were prepared by a typical solution-casting technique. Firstly, poly(vinylidene fluoride) (PVDF) and *N*,*N*-dimethylformamide (DMF) were stirred overnight with a mass ratio of 1 : 5 to obtain a clear gel solution. Then 3 g lithium aluminum titanium phosphate (LATP), 0.5 g lithium bis(trimethyl sulfonyl)imide (LiTFSI), and 0.15 g g-C_3N_4 were added into 3 g DMF solvent, and the mixture were vigorously stirred to obtain a uniform suspension. Subsequently, 6 g PVDF gel solution was added to the above suspension and stirred overnight. Finally, the obtained slurry was casted onto a PET film and dried it at 50 °C for 24 h to form a self-supporting film.[41]

Characterization

X-ray diffraction (XRD, Rigaku D/max-2500 diffraction meter with a Cu Kα radiation source) patterns were obtained for the phase identification of the prepared TNO powders. Microstructures of the TNO anodes were observed by scanning electron microscopy (SEM, ZEISS Gemini2). Elemental distribution of the TNO anodes were detected by energy dispersive X-ray spectroscopy (EDS, OxfordX-MAX) coupled with scanning electron microscopy.

Electrochemical measurements

CR2032 coin cells were assembled in an Ar-filled glovebox to evaluate the electrochemical performance of TNO anodes. The liquid state batteries service 1.0 M $LiPF_6$ in ethylene carbonate

(EC)/dimethyl carbonate (DMC)/ethyl methyl carbonate (EMC) mixture (in a 1 : 1 : 1 volume ratio) as the electrolyte, porous PE membrane (Celgard 2325) as a separator, Li metal as the counter electrode, and TNO electrode as the working electrode.

The solid state batteries employ $LATP_{CPEs}$ as the solid electrolyte, TNO-0.2C anodes as active electrodes, and Li metal as counter electrodes. A drop of 1.0 M $LiPF_6$-1 : 1 : 1 EC/DMC/EMC liquid electrolyte is added to reduce the interfacial impedance between the electrolyte and electrode during the battery assembly process.

The coin cells were charged and discharged using a LAND CT3002A battery test system at room temperature between 1.0 V and 3.0 V (*vs.* Li/Li^+). Cyclic voltammogram (CV) measurements were conducted on a PARSTAT MC multichannel electrochemical workstation in the potential range of 1.0–3.0 V at a scanning rate of 0.1 mV s^{-1}. Electrochemical impedance spectroscopy (EIS) was also performed on the same electrochemical workstation in the frequency range of 100 kHz to 100 mHz.

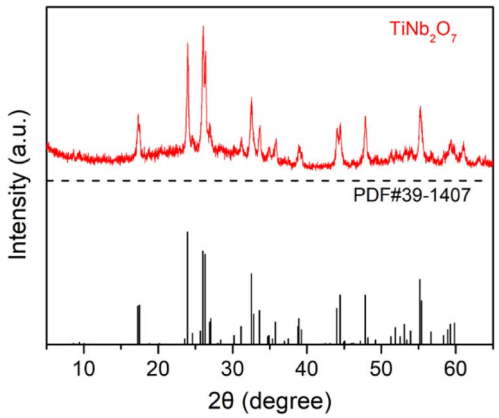

Fig. 1 XRD pattern of TNO powder.

Results and discussion

Fig. 1 shows the X-ray diffraction (XRD) pattern of the TNO powder. All diffraction peaks of the sample are consistent with the monoclinic $TiNb_2O_7$ phase (JCPDS: #39-1407). No diffraction peaks of Nb_2O_5 and TiO_2 are observed, indicating that pure-phase $TiNb_2O_7$ is obtained.

Fig. 2 displays the cross-section and surface morphology of the TNO-C anode by SEM. TNO particles exhibit irregular sphere-like shapes and possess particle-sizes concentrated on a distribution ranging from hundreds of nanometers to several micrometers. The average particle size (D_{50}) of TNO is 1.07 μm, as shown in Fig. S1 in the ESI.† In addition, the CNTs distribute around TNO particles in the form of filaments, which act as the "highway" of electronic transmission in the TNO composite anode. The CNTs distributed uniformly with the increase in the content of CNTs, as seen in Fig. 2a–d. Whereas, as the proportion of CNTs in the conductive agents reaches to 50 wt%, obviously agglomeration of CNTs was observed in Fig. 2f. The agglomeration of CNTs will weaken the enhancing effects on

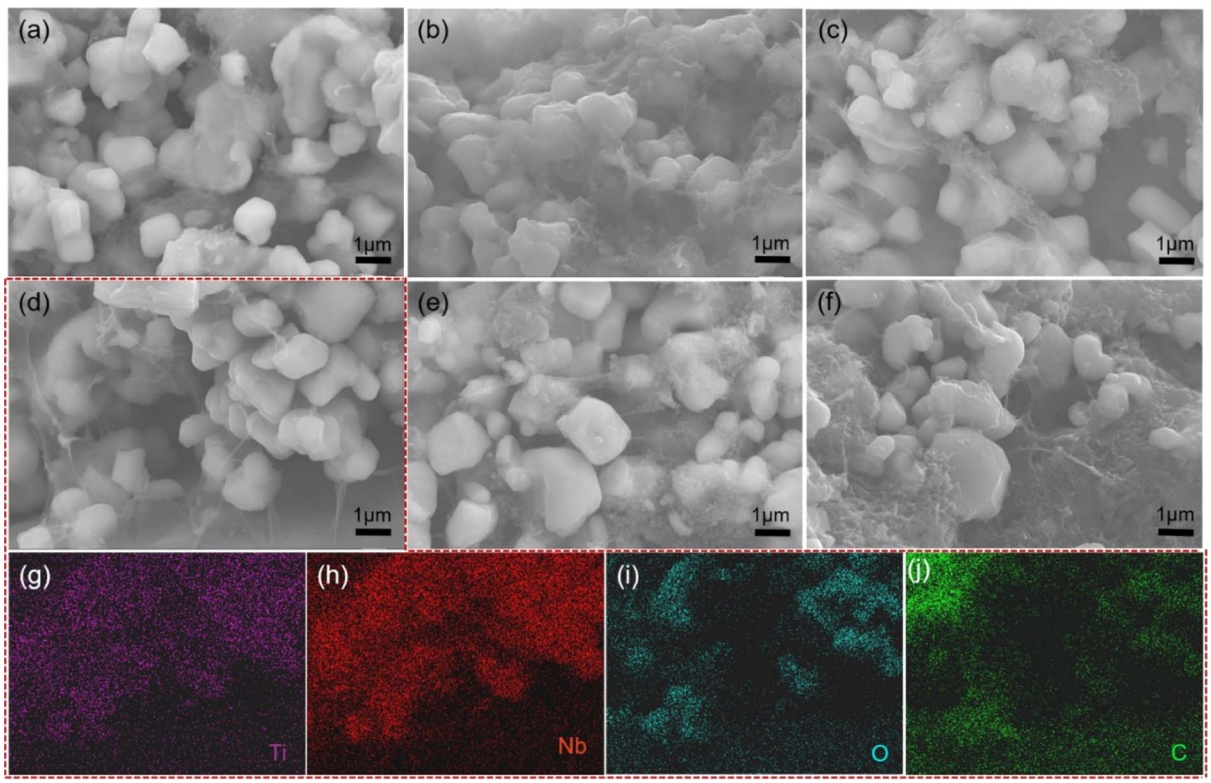

Fig. 2 Cross-section SEM images of (a) TNO-0.05C, (b) TNO-0.1C, (c) TNO-0.15C, (d) TNO-0.2C and (f) TNO-0.5C anodes, together with the top-view of (e) TNO-0.2C. EDS mapping images of (g) Ti, (h) Nb, (i) O and (j) C elements on (d) the cross-section of TNO-0.2C anode.

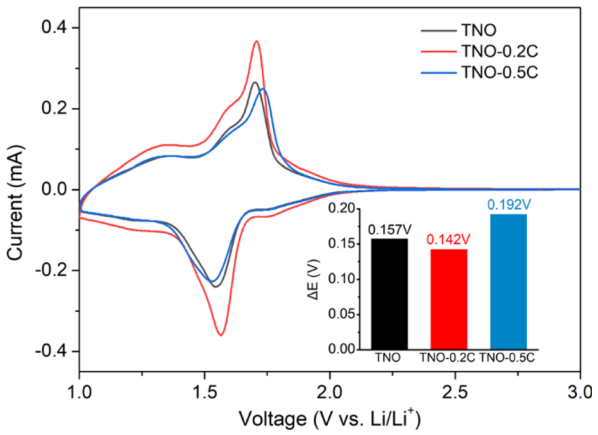

Fig. 3 Cyclic voltammetry curves of TNO, TNO-0.2C and TNO-0.5C between 1.0 and 3.0 V at 0.1 mV s^{-1}.

the electronic conductivity of the TNO composite anode and may also restrict the high-speed migration of Li^+. The EDS element mapping analysis is conducted on the cross-section of TNO-0.2C anode, as seen in Fig. 2d. Ti, Nb, O and C elements (Fig. 2g–j) distributed uniformly in the samples.

Raman spectra of the TNO powders are presented in Fig. S2a.† The characteristic peaks at 1000 cm^{-1} and 887 cm^{-1} correspond to the stretching vibrations of the edge/corner shared NbO_6 octahedra. The other peaks at 648 cm^{-1} and 539 cm^{-1} are attributed to the metal–oxygen stretching of TiO_6 octahedra. Furthermore, the band at 269 cm^{-1} is related to the symmetric and antisymmetric bending vibration of O–Ti–O and O–Nb–O. XPS spectra are conducted on TNO powders as shown in Fig. S2b–e.† Ti, Nb and O element are detected in the TNO sample, the peaks at 463.9 eV and 458.1 eV corresponding to Ti $2p_{1/2}$ and Ti $2p_{3/2}$, while the peaks at 209.6 eV and 206.9 eV attributing to Nb $3d_{3/2}$ and Nb $3d_{5/2}$, and the peaks at 529.6 eV relating to O 1s.

The cyclic voltammetry (CV) curves of TNO, TNO-0.2C and TNO-0.5C operated between 1.0 V and 3.0 V at a sweep rate of 0.1 mV s^{-1} are shown in Fig. 3. All of the three curves consist of a broad bump and a couple of sharp redox peaks. The broad bump distributed in the voltage of 1.0–1.4 V corresponds to the redox process of Nb^{4+}/Nb^{3+} and Ti^{4+}/Ti^{3+} couples, and the sharp redox peaks located at 1.706 V/1.549 V for TNO, 1.705 V/1.563 V for TNO-0.2C and 1.728 V/1.536 V for TNO-0.5C are contributed to the oxidation and reduction of the Nb^{5+}/Nb^{4+} couple. The polarization potential (ΔE) between the oxidation peaks and reduction peaks are presented in the inset of Fig. 3. The TNO-0.2C shows higher redox peak intensities and smaller potential interval between the reduction and oxidation peaks compared to the TNO sample, suggesting better reaction kinetics and smaller polarization. On the other hand, the TNO-0.5C anode presents smaller redox peak intensities and lager polarization compared to the TNO sample, which will restrict its electrochemical performance.

Fig. 4 displays the charge/discharge curves of TNO and TNO-C anodes at various rates. The voltage platforms for all TNO and TNO-C samples at 0.5C appear around 1.6–1.7 V, which corresponds well with the sharp oxidation and reduction peaks of Nb^{5+}/Nb^4 redox couple in Fig. 3. With the increase of the C-rate, polarization of the batteries with all TNO and TNO-C samples become larger, leading to more obvious voltage differences between charging and discharging platforms, as well as the decrease of charging/discharging capacities. In order to exhibit the enhancement effect of SP-CNT binary conductive agents

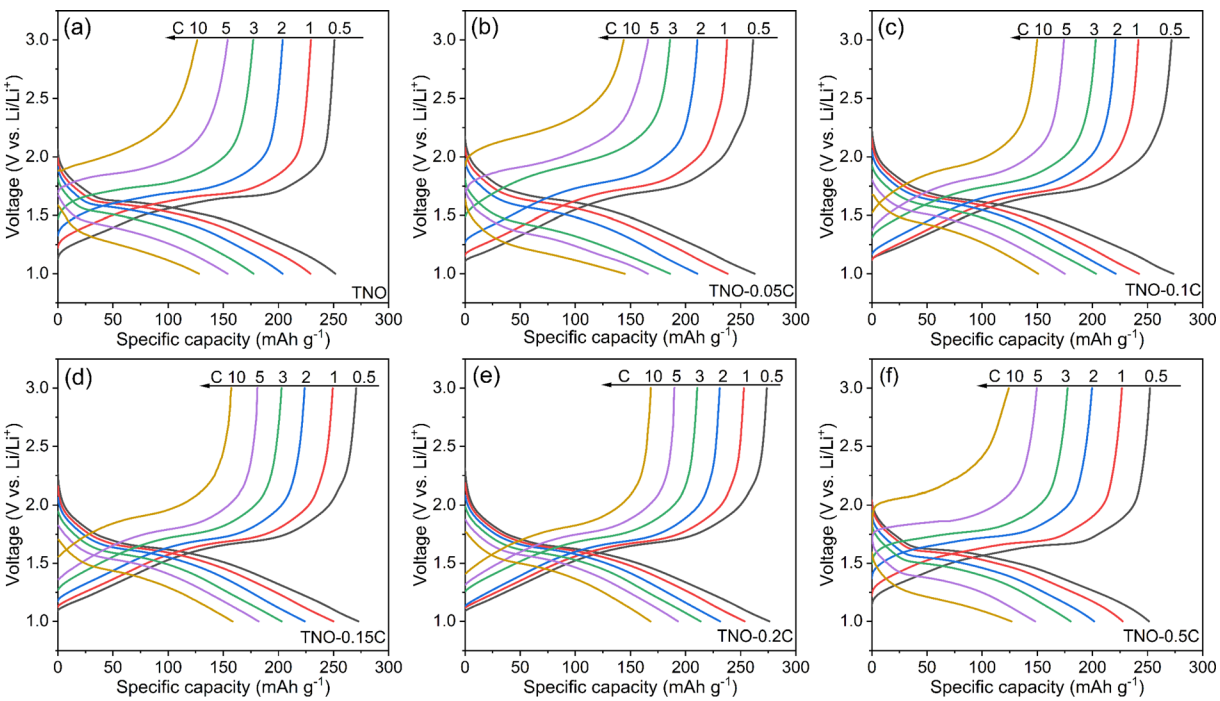

Fig. 4 Charge/discharge curves of (a) TNO, (b) TNO-0.05C, (c) TNO-0.1C, (d) TNO-0.15C, (e) TNO-0.2C and (f) TNO-0.5C at various rates.

more clearly, the histograms of discharge capacities of TNO samples are shown in Fig. S3 in the ESI.†

The TNO-0.05C, TNO-0.1C, TNO-0.15C and TNO-0.2C exhibit much better rate performance and larger discharge capacities than the TNO samples, due to the enhancing effects of the SP-CNT binary conductive agents on the electronic conductivities of the TNO composite anodes. In the SP-CNT binary conductive system, SP particles surround the TNO particles closely, serving as the short range passageways for electron migration.[36,42] Meanwhile, the CNTs filaments distribute uniformly in the electrodes and make bridge connections of the neighboring TNO particles, serving as the long range highways for the transportation of electrons.[36,43–45] The combination of the short range and long range conductive agents guarantee a high efficient electronic conductive network and bring better rate performances. Whereas, when the proportion of the CNTs reaches 50 wt% in the SP-CNT binary conductive system, *i.e.* for the TNO-0.5C sample, the excessive CNTs begin to aggregate together, as seen in Fig. 2f. The agglomeration of CNTs will weaken the enhancing effects on the electronic conductivity of the TNO composite anode and may also restrict the high-speed migration of Li^+. Thus, the optimized proportion of the CNTs in the SP-CNT binary conductive system is around 20 wt%, and the TNO-0.2C sample present the best rate performance.

Fig. 5a exhibits the rate performances of TNO and TNO-C anodes. The TNO sample delivers discharge capacities of 252, 228.8, 207.6, 180, 149.3 and 126.3 mA h g^{-1} at 0.5, 1, 2, 3, 5 and 10C, respectively. Meanwhile, the TNO-0.05C, TNO-0.1C, TNO-0.15C and TNO-0.2C exhibit much better rate performance than the TNO samples, as mentioned above. The TNO-0.2C sample presents the best discharge capacities of 278.6, 256, 231.9, 211.8, 192.3 and 178.1 mA h g^{-1} at 0.5, 1, 2, 3, 5 and 10C, respectively. That is, the discharge capacity of the TNO-0.2C increase over 30% at 10C than that of the TNO. Notability, the solid state synthesized TNO-0.2C sample reveals competitive rate capabilities with those reported works at moderate rates (ranging from 1C to 10C), which are perfectly adequate for large-scale applications. The properties comparison among reported TNO anodes and this work are listed in Table S1 in ESI.† In the contrast, the TNO-0.5C only possesses discharge capacities of 247.3, 225.5, 195.7, 174, 145.3 and 118.7 mA h g^{-1} at 0.5, 1, 2, 3, 5 and 10C, respectively, which are even worse than those of the TNO. Thus approximately 20 wt% is the optimized proportion of the CNTs in the SP-CNT binary conductive system, which ensures the best enhancing effect on the electrochemical electrodes. At the rate back to 0.5C, the discharge capacities of all the TNO and TNO-C almost recover to the capacity values before rate test, which proves the cycling stability of these solid state synthesized samples.

The cycling performance of TNO and TNO-C anodes are measured to further identify the lithium ion storage capability, as shown in Fig. 5b. The initial reversible discharge capacity of TNO at 1.5C/1.5C is 219.6 mA h g^{-1}, and the discharge capacity decays to 198.8 mA h g^{-1} after 200 cycles, corresponding to capacity retention of 90.5%. Meanwhile, the initial capacities of TNO-0.05C, TNO-0.1C, TNO-0.15C and TNO-0.2C anodes at 1.5C/1.5C are 225.4, 231.1, 231.5 and 241.7 mA h g^{-1} respectively, which are all higher than that of TNO anodes. And the capacity retention of TNO-0.05C, TNO-0.1C, TNO-0.15C and TNO-0.2C anodes after 200 cycles are 90.5%, 90.7%, 91.3% and 92.2%, which are roughly the same as that of TNO anodes. The excellent cycling performances of TNO and TNO-C root in the facile two-step solid state calcination method, which has been reported in our previous work.[40] Thus, the addition of the SP-CNT binary conductive agents into the TNO composite anodes can enhance the discharge capacity without deteriorating the cycling performance. And the TNO-0.2C shows the best cycling performance, corresponding well with the CV result and rate capability test above. Furthermore, the coulombic efficiency of TNO-0.2C anode is nearly 100% during the cycling, indicating an excellent electrochemical reversible kinetic process.

The electrochemical impedance spectroscopy (EIS) analyses of TNO, TNO-0.2C and TNO-0.5C anodes are shown in Fig. 6a. The Nyquist plots of all anodes consisted of a depressed semicircle in the high frequency region and an inclined straight line in the low frequency region. In Nyquist plots, the intersection of the curve and the real axis represents the ohmic resistance (R_s) of the cell. In the high frequency region, the diameter of the semicircle is equal to the charge transfer resistance (R_{ct}) between the electrolyte and the electrode. The slope of the

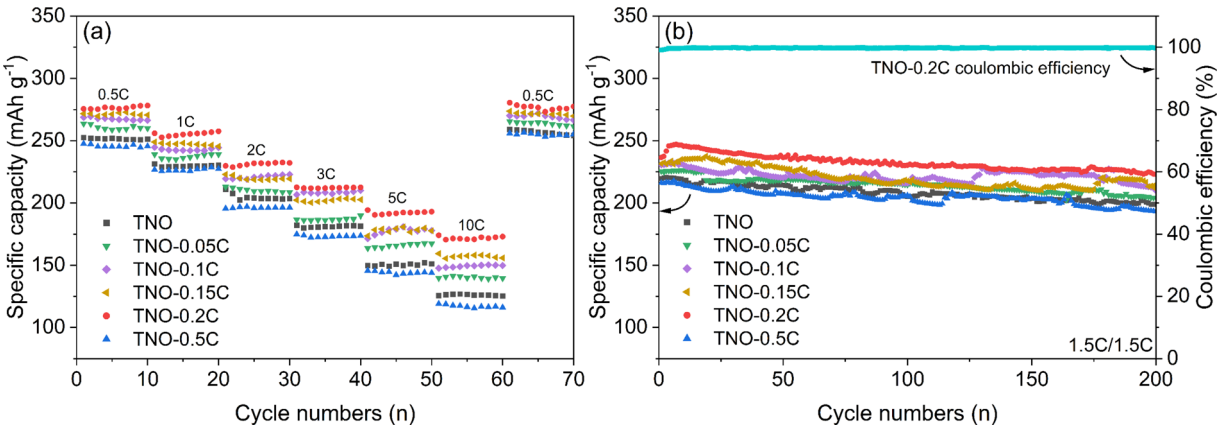

Fig. 5 (a) Rate performances of TNO and TNO-C, (b) cyclic performances of TNO and TNO-C at 1.5C/1.5C.

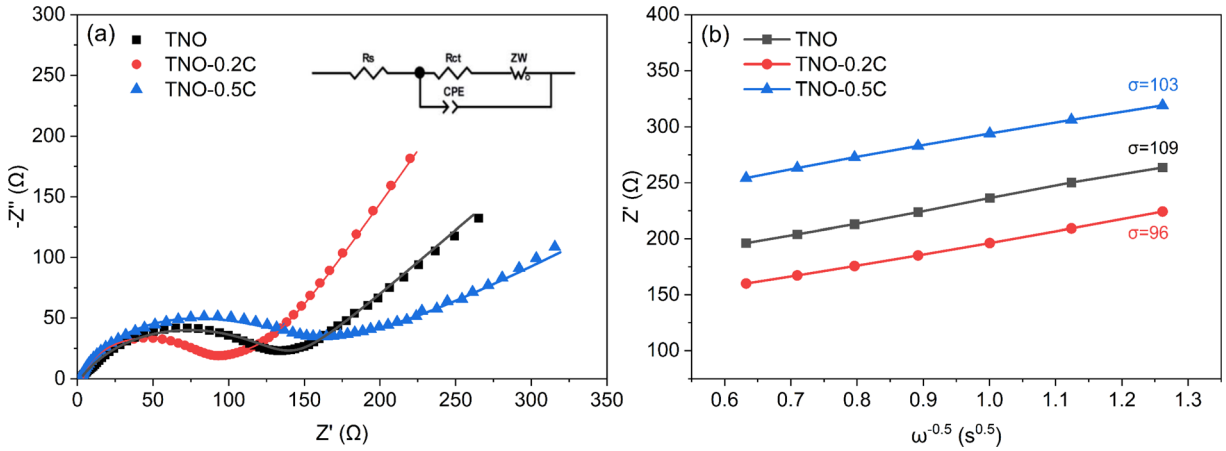

Fig. 6 (a) Nyquist plots of TNO, TNO-0.2C and TNO-0.5C, (b) the relationship between Z' and $\omega^{-0.5}$ at low frequency.

Table 1 Calculated values of the impedance and Li^+ diffusion coefficient from simulation data

Samples	R_s (Ω)	R_{ct} (Ω)	σ (Ω $s^{-0.5}$)	D (cm^2 s^{-1})
TNO	2.16	117.51	109	1.95×10^{-16}
TNO-0.2C	3.71	71.96	96	2.52×10^{-16}
TNO-0.5C	1.98	135.12	103	2.19×10^{-16}

inclined straight line in the low frequency region is related to the Warburg impedance, which reflects the Li^+ diffusion coefficient D of the active material. The D values can be obtained according to the following equations.

$$Z' = R_s + R_{ct} + \sigma\omega^{-0.5} \quad (1)$$

$$D = R^2T^2/(2A^2n^4F^4c^2\sigma^2) \quad (2)$$

herein, R, T, A, n, F, C, ω and σ represent the gas constant, the absolute temperature, the surface area of the electrode, the electron-transfer number, the Faraday constant, the molar concentration of Li^+, the angular frequency and the Warburg coefficient, which can be obtained from the slope of the Z'–$\omega^{-0.5}$ plots shown in Fig. 6b. The units of symbols in formulas (1) and (2) are listed in Table S2.†

Table 1 presents the values of R_s and R_{ct} simulated by Zview software, Warburg coefficient and Li^+ diffusion coefficient D calculated by formula (1) and (2). The ohmic resistance (R_s) of all the TNO samples are small. They are dominated by contact resistances and are of no practical significance. Meanwhile, the charge transfer resistance (R_{ct}) of the TNO-0.2C is much smaller than that of TNO, and the Li^+ diffusion coefficient D of the TNO-0.2C is higher than that of TNO, revealing that the TNO-0.2C has higher electronic conductivity and better reaction kinetics due to the addition of the SP-CNT binary conductive agents. Whereas the TNO-0.5C only presents better Li^+ diffusion coefficient D and worse charge transfer resistance (R_{ct}) than that of TNO, due to the aggregation of excessive CNTs, which restrict the high-speed migration of Li^+.

The solid state batteries (SSB) with Li metal as counter electrodes, modified LATP-based "polymer in ceramic" as composite polymer electrolytes[41] and TNO/TNO-0.2C anodes as active electrodes were assembled to study the feasibility of TNO anodes in solid state batteries. Fig. 7a displays the rate

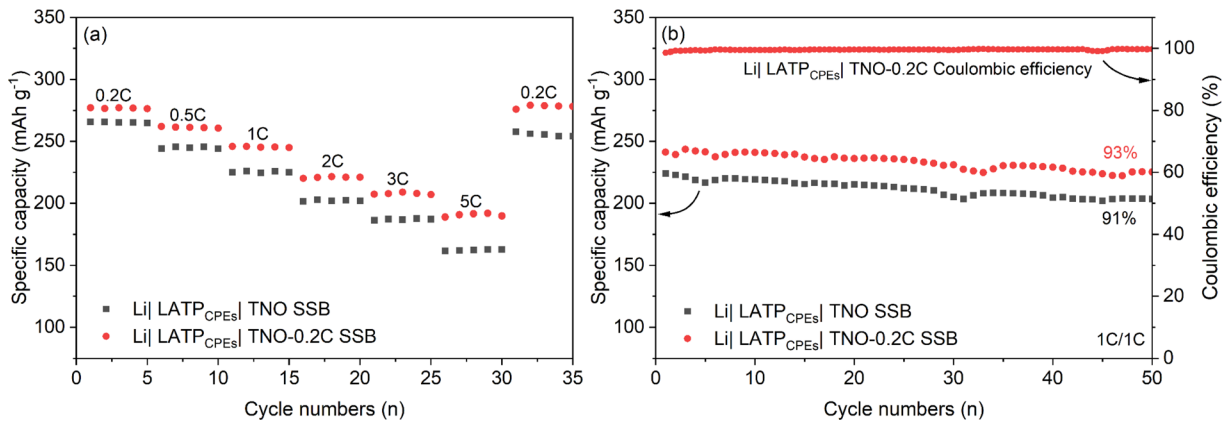

Fig. 7 (a) Rate performance of Li|$LATP_{CPEs}$|TNO SSB and Li|$LATP_{CPEs}$|TNO-0.2C SSB, (b) cyclic performances of Li|$LATP_{CPEs}$|TNO SSB and Li|$LATP_{CPEs}$|TNO-0.2C SSB at 1C/1C.

performances of the SSBs. The discharge capacities of Li|$LATP_{CPEs}$|TNO SSB at 0.2, 0.5, 1, 2, 3 and 5C are 265.8, 244.2, 224.8, 201.6, 186.4 and 161.7 mA h g^{-1}, respectively. In contrast, the Li|$LATP_{CPEs}$|TNO-0.2C SSB exhibits higher discharge capacities of 277.2, 262.1, 245.8, 220, 207.2 and 188.8 mA h g^{-1} at 0.2, 0.5, 1, 2, 3 and 5C, respectively. When the rate back to 0.2C, the discharge capacity of Li|$LATP_{CPEs}$|TNO-0.2C SSB returns to 276 mA h g^{-1}, indicating better rate capability and electrochemical reversibility than Li|$LATP_{CPEs}$|TNO SSB. The cyclic performances of TNO and TNO-0.2C SSBs are shown in Fig. 7b. The initial reversible discharge capacity of Li|$LATP_{CPEs}$|TNO SSB is 223.9 mA h g^{-1} at 1C, and the discharge capacity decays to 203.4 mA h g^{-1} after 50 cycles, corresponding to the capacity retention rate of 91%. While the Li|$LATP_{CPEs}$-|TNO-0.2C SSB delivers a higher initial reversible discharge capacity of 241.3 mA h g^{-1} at 1C and a better capacity retention rate of 93% after 50 cycles (with a discharge capacity of 225.2 mA h g^{-1}). And the coulombic efficiency of Li|$LATP_{CPEs}$-|TNO-0.2C SSB is nearly 100% during the cycling. The improved electrochemical performance of Li|$LATP_{CPEs}$|TNO-0.2C SSB indicates that the TNO-0.2C is a promising composite anode for solid state battery due to the efficient electronic conductive network constructed by long range and short range conductivity of SP-CNT binary conductive agents.

Conclusions

In this work, the SP-CNT binary conductive agent was utilized to enhance the electrochemical performances of solid state synthesized TNO anode. In the SP-CNT binary conductive system, SP distributed around TNO particles uniformly, acting as short range conductive pathways. While CNTs bridged adjacent TNO particles, acting as long range highways for transportation of electrons. The combination of long range and short range conductive agents construct an efficient electronic migration network, which significantly improves the electrochemical performance of TNO anodes. Whereas, excessive CNTs will aggregation together and restrict the rapid transfer of electrons, as seen in TNO-0.5C. Approximately 20 wt% is the optimized proportion of the CNTs in the SP-CNT binary conductive system. The TNO-0.2C anode exhibits a high reversible discharge capacity of 278.6 mA h g^{-1} at 0.5C, competitive rate capabilities at moderate rates (178.1 mA h g^{-1} at 10C), and an excellent capacity retention of 92.2% after 200 cycles at 1.5C/1.5C. The Li|$LATP_{CPEs}$|TNO-0.2C solid state batteries are also assembled, which deliver high initial reversible discharge capacity of 241.3 mA h g^{-1} at 1C and a good capacity retention rate of 93% after 50 cycles. The addition of the SP-CNT binary conductive agents is a high efficient way to improve the electrochemical properties of high-performance oxide composite electrode, especially for solid state batteries.

Conflicts of interest

The authors declare no competing financial interest.

Acknowledgements

The authors acknowledge the financial supports from the National Natural Science Foundation of China (Grant No. 52272131, 52171210), Natural Science Foundation of Jiangsu Province (Grant No. BK20210137), Fundamental Research Funds for the Central Universities (Grant No. 2023JCCXJD04), Yue Qi Young Scholar Project of China University of Mining & Technology (Beijing) (Grant No. 2019QN12), State Key Laboratory of New Ceramics and Fine Processing Tsinghua University (Grant No. KFZD201901, KF201910), Open Fund of State Key Laboratory of Coal Resources and Safe Mining (Grant No. SKLCRSM19KFA13), and Key Laboratory of Functional Materials Physics and Chemistry (Jilin Normal University), Ministry of Education, China (Grant No. 202401 and 202402).

Notes and references

1 J. M. Tarascon and M. Armand, *Nature*, 2001, **414**, 359–367.
2 D. Larcher and J. M. Tarascon, *Nat. Chem.*, 2015, **7**, 19–29.
3 K. S. Kang, Y. S. Meng, J. Breger, C. P. Grey and G. Ceder, *Science*, 2006, **311**, 977–980.
4 B. Kang and G. Ceder, *Nature*, 2009, **458**, 190–193.
5 V. Etacheri, R. Marom, R. Elazari, G. Salitra and D. Aurbach, *Energy Environ. Sci.*, 2011, **4**, 3243–3262.
6 N. Takami, K. Ise, Y. Harada, T. Iwasaki, T. Kishi and K. Hoshina, *J. Power Sources*, 2018, **396**, 429–436.
7 J. B. Goodenough and Y. Kim, *Chem. Mater.*, 2010, **22**, 587–603.
8 S. S. Zhang, *J. Power Sources*, 2006, **163**, 567–572.
9 Y. Sun, T. Sun, X. Lin, X. Tao, D. Zhang and C. Zeng, *Sci. China: Chem.*, 2018, **61**, 670–676.
10 B. K. Guo, X. Q. Yu, X. G. Sun, M. F. Chi, Z. A. Qiao, J. Liu, Y. S. Hu, X. Q. Yang, J. B. Goodenough and S. Dai, *Energy Environ. Sci.*, 2014, **7**, 2220–2226.
11 S. F. Lou, X. Q. Cheng, Y. Zhao, A. Lushington, J. L. Gao, Q. Li, P. J. Zuo, B. Q. Wang, Y. Z. Gao, Y. L. Ma, C. Y. Du, G. P. Yin and X. L. Sun, *Nano Energy*, 2017, **34**, 15–25.
12 Q. S. Cheng, J. W. Liang, Y. C. Zhu, L. L. Si, C. Guo and Y. T. Qian, *J. Mater. Chem. A*, 2014, **2**, 17258–17262.
13 F. P. Zhao, S. H. Alahakoon, K. Adair, S. M. Zhang, W. Xia, W. H. Li, C. Yu, R. F. Feng, Y. F. Hu, J. W. Liang, X. T. Lin, Y. Zhao, X. F. Yang, T. K. Sham, H. Huang, L. Zhang, S. Q. Zhao, S. G. Lu, Y. N. Huang and X. L. Sun, *Adv. Mater.*, 2021, **33**, 2006577.
14 W. Z. Huang, N. Matsui, S. Hori, K. Suzuki, M. Hirayama, M. Yonemura, T. Saito, T. Kamiyama, Y. Sasaki, Y. Yoon, S. Kim and R. Kanno, *J. Am. Chem. Soc.*, 2022, **144**, 4989–4994.
15 X. N. Li, J. W. Liang, J. Luo, M. N. Banis, C. H. Wang, W. H. Li, S. X. Deng, C. Yu, F. P. Zhao, Y. F. Hu, T. K. Sham, L. Zhang, S. Q. Zhao, S. G. Lu, H. Huang, R. Y. Li, K. R. Adair and X. L. Sun, *Energy Environ. Sci.*, 2019, **12**, 2665–2671.
16 X. N. Li, J. W. Liang, N. Chen, J. Luo, K. R. Adair, C. H. Wang, M. N. Banis, T. K. Sham, L. Zhang, S. Q. Zhao, S. G. Lu,

H. Huang, R. Y. Li and X. L. Sun, *Angew. Chem., Int. Ed.*, 2019, **58**, 16427–16432.
17 R. DeWees and H. Wang, *ChemSusChem*, 2019, **12**, 3713–3725.
18 R. X. Lv, W. J. Kou, S. Y. Guo, W. J. Wu, Y. T. Zhang, Y. Wang and J. T. Wang, *Angew. Chem., Int. Ed.*, 2022, **61**, e202114220.
19 S. J. Deng, H. Zhu, B. Liu, L. Yang, X. L. Wang, S. H. Shen, Y. Zhang, J. A. Wang, C. Z. Ai, Y. Ren, Q. Liu, S. W. Lin, Y. F. Lu, G. X. Pan, J. B. Wu, X. H. Xia and J. P. Tu, *Adv. Funct. Mater.*, 2020, **30**, 2002665.
20 M. Liu, H. C. Dong, S. Zhang, X. Chen, Y. P. Sun, S. Gao, J. Q. Xu, X. D. Wu, A. B. Yuan and W. Lu, *Chemelectrochem*, 2019, **6**, 3959–3965.
21 H. Noh and W. Choi, *J. Electrochem. Soc.*, 2016, **163**, A1042–A1049.
22 S. Lou, X. Cheng, J. Gao, Q. Li, L. Wang, Y. Cao, Y. Ma, P. Zuo, Y. Gao, C. Du, H. Huo and G. Yi, *Energy Storage Mater.*, 2018, **11**, 57–66.
23 X. H. Xia, S. J. Deng, S. S. Feng, J. B. Wu and J. P. Tu, *J. Mater. Chem. A*, 2017, **5**, 21134–21139.
24 L. Fei, Y. Xu, X. F. Wu, Y. L. Li, P. Xie, S. G. Deng, S. Smirnov and H. M. Luo, *Nanoscale*, 2013, **5**, 11102–11107.
25 C. Yang, S. Yu, Y. Ma, C. F. Lin, Z. H. Xu, H. Zhao, S. Q. Wu, P. Zheng, Z. Z. Zhu, J. B. Li and N. Wang, *J. Power Sources*, 2017, **360**, 470–479.
26 C. R. Lei, X. Qin, S. Y. Huang, T. Y. Wei and Y. Z. Zhang, *Chemelectrochem*, 2021, **8**, 3379–3383.
27 K. Liu, J. A. Wang, J. Yang, D. Q. Zhao, P. Y. Chen, J. Z. Man, X. Y. Yu, Z. Q. Wen and J. C. Sun, *Chem. Eng. J.*, 2021, **407**, 127190.
28 M. Qi, D. Chao, W. Sun, J. Yin and M. Chen, *RSC Adv.*, 2020, **10**, 6342–6350.
29 Y. Yang, Y. Yue, L. Wang, X. F. Cheng, Y. T. Hu, Z. Z. Yang, R. X. Zhang, B. Jin and R. X. Sun, *Int. J. Hydrogen Energy*, 2020, **45**, 12583–12592.
30 C. F. Lin, L. Hu, C. B. Cheng, K. Sun, X. K. Guo, Q. Shao, J. B. Li, N. Wang and Z. H. Guo, *Electrochim. Acta*, 2018, **260**, 65–72.
31 Y. K. Park, G. G. Park, J. G. Park and J. W. Lee, *Electrochim. Acta*, 2017, **247**, 371–380.
32 H. Song, Y. Oh, N. Cakmakci and Y. Jeong, *RSC Adv.*, 2019, **9**, 40883–40886.
33 N. Nitta, F. X. Wu, J. T. Lee and G. Yushin, *Mater. Today*, 2015, **18**, 252–264.
34 M. Hu, X. L. Pang and Z. Zhou, *J. Power Sources*, 2013, **237**, 229–242.
35 X. B. Zhang, J. Ma and K. Z. Chen, *Nano-Micro Lett.*, 2015, **7**, 360–367.
36 K. Wang, Y. Wu, S. Luo, X. F. He, J. P. Wang, K. L. Jiang and S. S. Fan, *J. Power Sources*, 2013, **233**, 209–215.
37 J. Y. Zhang, Z. Y. Huang, C. G. He, J. L. Zhang, P. Mei, X. Y. Han, X. G. Wang and Y. K. Yang, *Nanotechnol. Rev.*, 2020, **9**, 934–944.
38 S. E. Cheon, C. W. Kwon, D. B. Kim, S. J. Hong, H. T. Kim and S. W. Kim, *Electrochim. Acta*, 2000, **46**, 599–605.
39 M. H. Cao, L. Y. Wang, Q. Zhang, H. Zhang, S. W. Zhong and J. Chen, *Mater. Today Commun.*, 2023, **36**, 106677.
40 L. Q. Cheng, Y. J. He, K. Chen, Z. H. Ma, R. P. Liu, N. Liu and Y. C. Deng, *J. Mater. Chem. A*, 2022, **10**, 17586–17592.
41 X. X. Hao, K. Chen, Y. P. Tang, X. J. Zhong and K. F. Cai, *J. Alloys Compd.*, 2023, **942**, 169064.
42 L. Z. Wen, L. Wang, Z. W. Guan, X. M. Liu, M. J. Wei, D. H. Jiang and S. X. Zhang, *Ionics*, 2022, **28**, 3145–3153.
43 X. Y. Liu, W. H. Chen, Y. J. Xia and Q. Li, *J. Mater. Sci.: Mater. Electron.*, 2022, **33**, 21311–21320.
44 X. D. Zhu, J. Tian, S. R. Le, N. Q. Zhang and K. N. Sun, *Mater. Lett.*, 2013, **97**, 113–116.
45 J.-S. Yun, B. Jang, S.-S. Kim and H.-Y. Kim, *J. Korean Inst. Electr. Electron. Mater. Eng*, 2019, **32**, 179–186.